

Quasilinear magnetoresistance and de Haas–van Alphen quantum oscillations in a LuPb₂ single crystal

Feng Yang,¹ Shilong Li,¹ Shengwei Chi,¹ Xiaoxu Wang,¹ Shan Jiang,¹ Huakun Zuo,¹
Lingxiao Zhao,^{2,*} Gang Xu,^{1,3,4} and Zengwei Zhu^{1,†}

¹Wuhan National High Magnetic Field Center and School of Physics, Huazhong University of Science and Technology, Wuhan 430074, China

²Quantum Science Center of Guangdong-HongKong-Macao Greater Bay Area, Shenzhen 523335, China

³Institute for Quantum Science and Engineering, Huazhong University of Science and Technology, Wuhan 430074, China

⁴Wuhan Institute of Quantum Technology, Wuhan 430074, China



(Received 13 October 2022; revised 4 May 2023; accepted 8 June 2023; published 19 July 2023)

Materials with square lattices composed of group IV or V elements provide a promising platform for topological phases to emerge. We present the study on single crystals of LuPb₂, which is a compound based on the Pb square net. The de Haas–van Alphen effect measurements reveal clear quantum oscillations, from which nonzero Berry phases are extracted. DFT calculation confirmed the presence of anisotropic Dirac dispersion near Fermi energy, suggesting that LuPb₂ is a candidate Dirac semimetal. Additionally, LuPb₂ shows a large quasilinear magnetoresistance. Through analysis of the magnetotransport data, we have determined that the quasilinear magnetoresistance is primarily governed by the average carrier mobility, as predicted by the classic Parish-Littlewood model. Furthermore, we observed the surface superconductivity, with a highly anisotropic upper critical field and enhancement of the resistivity critical field, which we attributed to the presence of a potential nanoscale lead layer on the surface of the sample. These findings are expected to provide a new platform for hosting anisotropic Dirac fermions and superconductivity.

DOI: [10.1103/PhysRevB.108.035137](https://doi.org/10.1103/PhysRevB.108.035137)

I. INTRODUCTION

Materials with square-net structures have attracted significant attention in recent years due to their exotic topological properties [1]. Notable examples include XMnBi₂ compounds ($X = \text{Ca, Sr, Ba}$) [2–5], ZrSiM compounds ($M = \text{S, Se, Te}$) [6–8], and RSn₂ compounds ($R = \text{Y, Lu, Sc}$) [9–12]. These two-dimensional electronic structures have played a crucial role in discovering topological semimetals. Notably, square nets in crystal structure also make significant contributions to superconductivity. In cuprate superconductors, they are thought to be responsible for the extremely high superconducting transition temperature [13]. Recently, an increasing number of square-net superconductors have been identified [14–16], indicating that these materials may provide a promising avenue for discovering novel topological phases and emerging phenomena. Thus, square-net materials present a promising avenue for research in these areas.

Magnetoresistance, the change in electrical resistance of a material in response to an applied magnetic field, is a crucial phenomenon in modern condensed matter physics [17]. Linear magnetoresistance (LMR), a type of magnetoresistance characterized by a linear increase in resistance with magnetic field strength, has emerged as an intriguing deviation from the typical quadratic behavior observed in most metals and

semimetals [18,19]. LMR has been observed in a diverse range of materials, ranging from disordered systems such as bismuth thin films [20], InSb [21], and Ag_{2– δ} X [22–25], to topological semimetals like γ -PtBi₂ [26], YPdBi [27], TaAs [28], Na₃Bi [29], and Cd₃As₂, as well as topological insulators such as Bi₂Te₃ [30]. The underlying physical mechanisms behind LMR in these materials have been subject to extensive debate among researchers. Abrikosov proposed a quantum LMR mechanism that arises when the magnetic field strength approaches the quantum limit [30,31], while Parish and Littlewood proposed a classical mechanism based on spatial fluctuations in charge-carrier mobility in silver chalcogenides [22,32]. In addition, other factors have been implicated in LMR, including open Fermi surfaces [26], Hall fields [33], and carrier density fluctuations [34]. These proposed mechanisms highlight the complexity of LMR in semimetals. Further research is needed to fully understand the mechanisms behind LMR and to explore its potential applications in various fields.

In this study, we synthesized single crystals of LuPb₂ and studied their electronic band structure. Our analysis of de Haas–van Alphen (dHvA) quantum oscillations through torque measurements revealed the presence of multiple Fermi pockets and a nontrivial Berry phase. Theoretical calculations suggest that this compound is a topological semimetal. Moreover, our transport experiment demonstrated a large quasilinear MR at low temperature. We also observed superconductivity in this system, characterized by a significant anisotropy of the upper critical field and an enhancement of the resistivity critical field.

*zhaolx@mail.sustech.edu.cn

†zengwei.zhu@hust.edu.cn

II. EXPERIMENT

LuPb₂ single crystals were synthesized using the Pb-flux method. Lu and Pb pieces with a molar ratio of Lu:Pb = 1:20 were loaded into an alumina crucible, sealed in a quartz tube under a low-pressure argon gas environment, and then heated to 600 °C. After maintaining this temperature for 6 hours, the tube was slowly cooled to 450 °C in 150 hours, and excess flux was removed in a centrifuge. The grown crystals typically had dimensions of 1×3×0.2 mm³. Elemental analysis was carried out using inductively coupled plasma-optical emission spectrometry (Agilent ICP-OES730), while powder x-ray diffraction (XRD) measurements were performed at room temperature using a PANalytical X'Pert3 powder diffractometer with Cu-K radiation. Resistivity and heat capacity measurements were carried out using a Quantum Design physical property measurement system with a standard four-probe method adopted for resistivity measurements.

The dHvA effect was measured using a homemade cantilever torque magnetometer. The deflection of the cantilever resulting from the magnetic torque was measured in capacitance using an Andeen-Hagerling 2550A automatic capacitance bridge, with a capacitance measurement resolution of $\Delta C = 0.03$ fF. When the magnetization \vec{M} and magnetic field \vec{B} were confined to the xz plane, the torque was calculated as $\vec{\tau} = \vec{M} \times \vec{B} = (M_z B_x - M_x B_z) \hat{y}$. In paramagnetic materials such as LuPb₂, the torque formula can be rewritten as $|\vec{\tau}| = \Delta\chi B^2 \sin\phi \cos\phi$, where ϕ is the tilt angle of \vec{B} away from the \hat{z} axis, and $\Delta\chi = \chi_z - \chi_x$ is the magnetic susceptibility anisotropy. The longest crystalline b axis of LuPb₂ was oriented along the \hat{z} axis in our measurement.

The first-principles calculation for LuPb₂ is based on density functional theory (DFT) [35], within the Perdew-Burke-Ernzerhof (PBE) [36] exchange correlation implemented in the Vienna *ab initio* simulation package (VASP) [37,38]. The semilocal generalized gradient approximation (GGA) with the PBE parametrization was utilized to account for exchange-correlation effects. The self-consistent inclusion of spin-orbit coupling (SOC) was also considered in our calculations. The plane wave cutoff energy is 350 eV with a k mesh of $7 \times 7 \times 13$ for self-consistent calculations. Maximally localized Wannier functions are utilized to derive the tight-binding model [39] of bulk LuPb₂, which is subsequently employed for the calculation of the Fermi surface (FS). WannierTools [40] was used to calculate the topological properties of this system.

III. RESULTS AND DISCUSSION

A. Crystal structure

Figure 1(a) shows the crystal structure of LuPb₂, which belongs to the ZrSi₂-type family. This structure can be understood as an alternating arrangement of a square planar Pb atomic layer and a corrugated square lattice of Lu and Pb. As depicted in Fig. 1(b), the square net of the Pb planar layer exhibits slight distortion, with a bonding angle of approximately 90.51°. Consequently, the Pb atomic layers manifest a subtle corrugation in the ac plane, as shown in Fig. 1(c). Figure 1(d) displays the x-ray diffraction (XRD) patterns of a LuPb₂ single crystal, in which the peaks can be indexed as

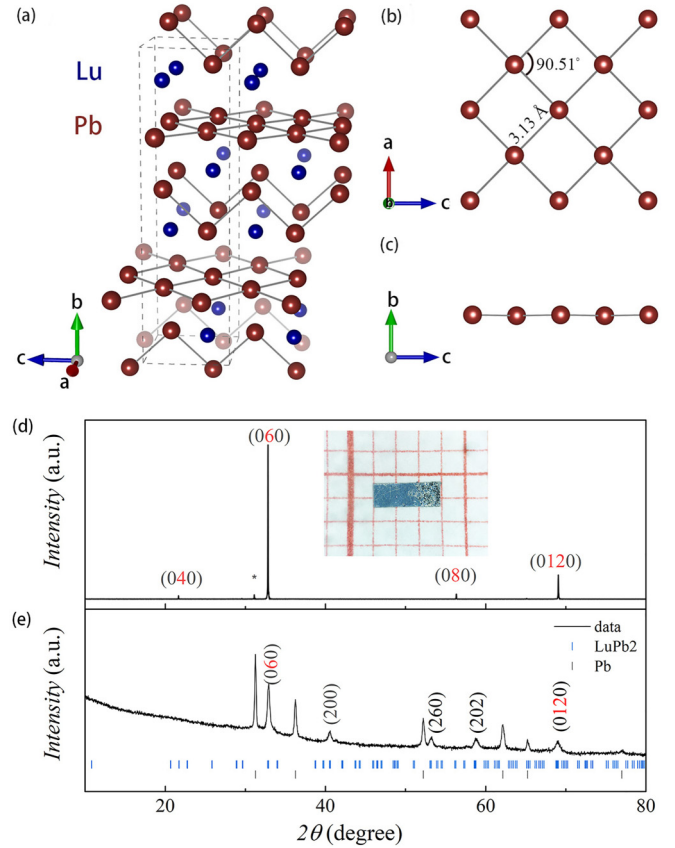


FIG. 1. (a) Crystal structure of LuPb₂. The blue and red balls represent the Lu and Pb atoms, respectively. (b) Top view of Pb plane. (c) Side view of the slightly distorted Pb square net layer. (d) Single-crystal x-ray-diffraction spectra of LuPb₂. Inset shows the optical image of a typical single crystal placed on a millimeter grid. (e) Powder XRD results at room temperature.

(010) reflections, indicating a preferred orientation along the b axis. Notably, a small peak resulting from the remnant Pb flux is observed in the XRD pattern and denoted by an asterisk.

Figure 1(e) displays the powder x-ray diffraction patterns of LuPb₂. Apart from the peaks attributed to Pb impurities, all the diffraction peaks can be indexed to an orthorhombic phase with the space group $Cmcm$. The obtained lattice parameters are $a = 4.450$ Å, $b = 16.369$ Å, and $c = 4.448$ Å. To determine the content of excess lead in the sample, we conducted an elemental analysis using inductively coupled plasma atomic emission spectroscopy (ICP-OES) measurements, as presented in Table I. The results indicate that excess lead is present in all three samples, both on the surfaces and inside the samples, which is consistent with previous reports [41]. The excess lead mainly aggregates on the surfaces

TABLE I. The elemental analysis of the product by ICP-OES.

Sample	Pb:Lu atomic ratio	Is the surface flux cleaned?
4	2.089	Yes
5	2.220	Yes
6	2.581	No

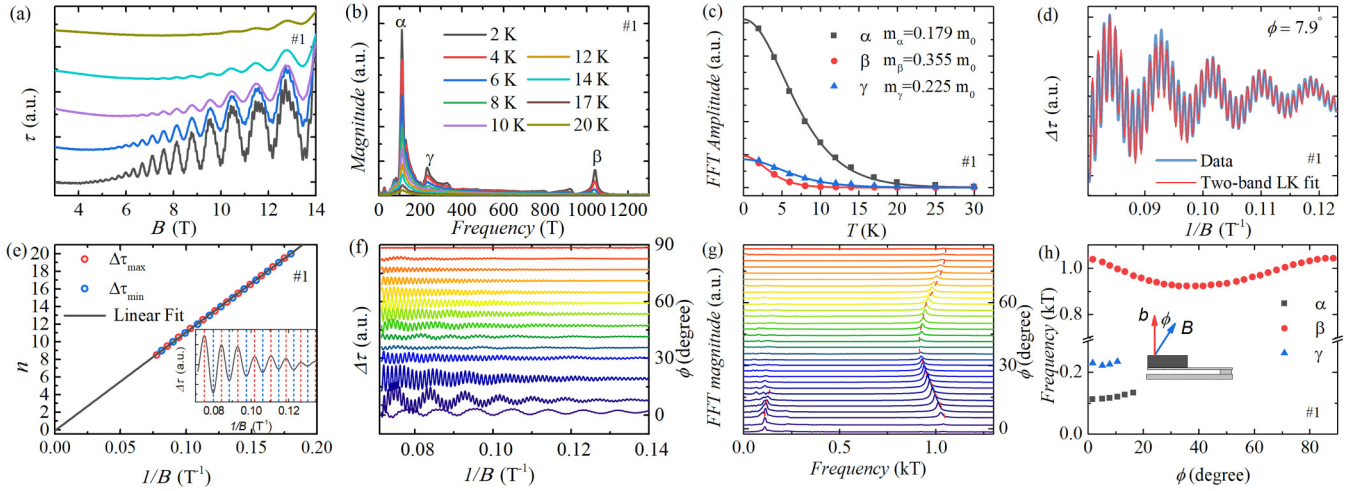


FIG. 2. (a) Magnetic field dependence of magnetic torque τ at various temperatures with B along the b axis. The curves have been shifted for clarification. (b) The FFT spectra of dHvA oscillations at different temperatures. (c) Temperature dependence of the FFT amplitudes for α and β band. The solid lines are the LK fits for the effective mass. (d) The oscillatory part of the $\Delta\tau$ dependence of $1/B$ at $\theta = 7.9^\circ$. The blue line is the experimental data, and the red line is the fit by the two-band LK formula. (e) Landau level fan diagram for α band. The solid line is the linear extrapolated fit. The inset shows the filtered wave of the α band. (f) dHvA oscillations as a function of $1/B$ at various angles. (g) The FFT spectra of the dHvA at different angles. (h) The angular dependence of the oscillation frequencies. The inset shows the schematic of the measurement configuration with the angle ϕ between the applied field B and the b axis.

of the samples, which are imperceptible to the naked eye. However, due to the excess lead and the sample's sensitivity to air, determining the crystal structure of LuPb₂ remains challenging [41,42]. To minimize these effects, we polished the surfaces of the measured samples and estimated the excess lead in the bulk to be within 8.17%–18.03%.

B. de Haas–van Alphen oscillations

Magnetic torque measurement is a fundamental experimental technique that provides insight into the electronic properties of materials. Figure 2(a) displays the isothermal magnetic torque τ with the magnetic field along the b axis at various temperatures. At a field as low as 3 T and 2 K, quantum oscillations are observed, indicating a high quality of the single crystal grown with a magnetic length of $l_B \approx 15$ nm. By the criterion $\mu B > 1$, we estimate the mobility μ to be larger than $0.33 \text{ m}^2 \text{ V}^{-1} \text{ s}^{-1}$. The quantum oscillations persist up to 20 K, implying that the bands have light effective masses. After the fast Fourier transform (FFT) analysis of the dHvA oscillations in the inverse magnetic field, three fundamental frequencies are extracted, as shown in Fig. 2(b). Specifically, two low frequencies $F_\alpha = 111$ T, $F_\gamma = 233$ T, and one high frequency $F_\beta = 1041$ T are identified. Notably, these frequencies are lower than those reported for pure lead, indicating that the quantum oscillations arise from LuPb₂ rather than lead inclusions [43,44]. According to the Onsager relation $F = \frac{\Phi_0}{2\pi^2} A_F$, we calculate the corresponding cross-sectional areas of the Fermi surface, which occupy 0.5%, 5.0%, and 11.1% of the $k_a k_c$ in the plane of the Brillouin zone for the α , γ , and β bands, respectively. The corresponding Fermi momentum $k_F = (\frac{A_F}{\pi})^{1/2}$, the Fermi velocity $v_F = \frac{\hbar k_F}{m^*}$, and the

volume carrier density $n_q = \frac{k_F^3}{3\pi^2}$ are calculated and listed in Table II.

Generally, the quantum oscillation amplitude of magnetic torque $\Delta\tau$ can be described by the Lifshitz-Kosevich (LK) formula [45,46],

$$\Delta\tau \propto -B^{3/2} R_T R_D R_S \sin \left[2\pi \left(\frac{F_s}{B} + \frac{1}{2} - \frac{\phi_B}{2\pi} - \delta \right) \right], \quad (1)$$

where $R_T = \lambda T / \sinh(\lambda T)$ is the temperature damping factor, where $\lambda = 2\pi^2 k_B \mu / \hbar e B$, $\mu = m^*/m_0$. Here, m_0 , \hbar , and e are

TABLE II. Parameters for Fermi pockets of LuPb₂ derived from the analyses of quantum oscillations. The F_s , m/m_e , A_F^i , k_F , v_F , n_q , T_D , l , μ_q , and ϕ_B are the quantum oscillation frequency, effective mass, Fermi cross section, Fermi wave vector, Fermi velocity, Dingle temperature, mean-free path, quantum mobility, and Berry phase of the extreme cross section of Fermi pocket, respectively.

Branch	α	γ	β
F_s (T)	111	233	1041
m^*/m_0	0.179	0.225	0.355
A_F (10^{-2} \AA^{-2})	1.06	2.22	9.94
k_F (\AA^{-1})	0.058	0.084	0.178
v_F (10^6 m/s)	1.27	1.65	1.98
n_q (10^{18} cm^{-3})	6.6	20.0	190.5
T_D (K)	30.03		33.94
l (nm)	5.1		7.1
μ_q ($\text{cm}^2 \text{ V}^{-1} \text{ s}^{-1}$)	1323		600
ϕ_B (LK $\delta = -\frac{1}{8}$)	1.02π		0.65π
ϕ_B (LK $\delta = \frac{1}{8}$)	0.52π		0.15π
ϕ_B (LL fan $\delta = -\frac{1}{8}$)	1.05π		
ϕ_B (LL fan $\delta = \frac{1}{8}$)	0.53π		

the free-electron rest mass, reduced Planck constant, and the charge of the bare electron, respectively. $R_D = \exp(-\lambda T_D)$ is the Dingle damping factor, and $R_S = \cos(\pi g\mu/2)$ is the spin-damping factor. The sine function term contains the Berry phase ϕ_B , and the additional phase shift $\delta = 0$ (2D system) or $\pm 1/8$ (+ and - for the minimum or maximum cross section of the Fermi surface in 3D systems, respectively) [10,11]. The temperature-dependent FFT amplitude can be well fitted by the thermal factor R_T as shown in Fig. 2(c). Due to the fact that the amplitude of the FFT is employed as the amplitude of the oscillation for the fitting shown in Fig. 2(b), it is necessary to substitute the field B in R_T with the average field $\bar{B} = 2/(1/B_{\text{start}} + 1/B_{\text{end}})$, where $B_{\text{start}} = 6$ T and $B_{\text{end}} = 14$ T. From the fitting, we extracted the cyclotron effective cyclotron masses $m_\alpha = (0.179 \pm 0.0011)m_0$, $m_\gamma = (0.225 \pm 0.0033)m_0$, and $m_\beta = (0.355 \pm 0.0027)m_0$, respectively. The calculated effective masses m^* for LuPb₂ are comparable to the previous report in YSn₂ ($0.023m_0$ – $0.082m_0$) [9], LuSn₂ ($0.053m_0$ – $0.06m_0$) [10], ScSn₂ ($0.04m_0$ – $0.054m_0$) [11], and ZrSiS ($0.11m_0$ – $0.27m_0$) [47].

To gain insight into the topological properties of the charge carriers, we performed Berry phase analyses on the dHvA oscillations using Eq. (1). As the dHvA oscillation comprises two primary frequencies α and β , we fitted the experimental data using the two-band LK formula, as shown in Fig. 2(d). The LK fitting revealed a phase factor of $(1/2 - \phi_B/2\pi - \delta) = 0.30$ for the β band, with $\phi_B = 0.15\pi$ for ($\delta = 1/8$) and 0.65π for ($\delta = -1/8$). Similarly, the phase factor for the α band was determined to be 0.116, which gives a Berry phase of $\phi_B = 0.52\pi$ for $\delta = 1/8$ and 1.02π for $\delta = -1/8$. The phase factor of 0.116 between $-1/8$ and $1/8$. Additionally, we used the oscillation pattern fit to determine the Dingle temperatures for the α and β pockets, which were found to be 30.03 K and 33.94 K, respectively. The corresponding quantum mean-free path $l_q = \frac{v_F \hbar}{2\pi k_B T_D}$ and quantum mobility $\mu_q = \frac{e\hbar}{2\pi k_B T_D m^*}$ were then calculated and are listed in Table II.

To investigate the potential topological character of the α band, we also determined the Berry phase from the Landau Level (LL) fan diagram. First, we separated the $\Delta\tau$ frequency via a filtering process and assigned the minima of $\Delta\tau$ to the Landau level index n , following the method described in Ref. [48]. The inset of Fig. 4(e) shows the $\Delta\tau$ dependence of $1/B$ for the α band. The plot of n versus the inverse field $1/B$ is displayed in Fig. 4(e), from which we could obtain the Berry phase $\phi_B = 2\pi(n_0 - \delta + 1/2)$, where $\delta = \pm 1/8$. The extrapolation of the linear fit in the fan diagram yields an intercept of $n_0 = -0.10$, which leads to a Berry phase of 0.55π for $\delta = 1/8$ and 1.05π for $\delta = -1/8$. This value is in good agreement with the value determined from the two-band LK fitting and provides further evidence of the potential topological character of the α band. However, it is essential to recognize that the relationship $\phi_B \sim \pi$ may not consistently serve as a sole indicator for the nontrivial topological features of Fermi pockets. This is due to the influence of factors such as symmetry, the position of extremal orbits, and various nongometric phase shifts [49,50]. Therefore, in the following text, we have provided additional evidence from DFT calculations of LuPb₂ to further support the conclusion.

To investigate the Fermi surface in LuPb₂, we measured the field dependence of the dHvA oscillations at various angles

ranging from the $B \parallel b$ axis to the $B \parallel a$ axis at a temperature of 2 K. Figure 2(f) displays the inverse field $1/B$ dependence of the dHvA oscillation $\Delta\tau$ after background subtraction at specific angles, which were shifted in 3° increments from 0° to 90° for clarity. The angle ϕ was defined as the angle between the direction of the field B and the b axis. Corresponding FFT spectra at different angles are shown in Fig. 2(g). The β band, exhibiting the highest oscillation frequency of 1041 T, was observed at all angles ranging from 0° to 90° and demonstrated significant angular dependence, implying a mildly anisotropic 3D Fermi surface, as shown in Fig. 2(h). In contrast, the other oscillation frequencies α and γ were detectable up to approximately 17° but vanished beyond this angle, suggesting potential open orbits or reduced carrier mobility as the angle inclined.

C. Electronic band structure

To further explore the topological properties of LuPb₂, we conducted first-principles calculations. Figure 3(a) shows the electronic band structure along the high-symmetry path direction without considering spin-orbit coupling effects. The red circle highlights the crossing points P_1 and P_2 near the Fermi energy (E_F). However, once spin-orbit coupling is considered, a gap of 75 meV opens at point P_1 due to the crossing bands belonging to the same irreducible representation of the point group, as depicted in Fig. 3(b). However, the crossing point P_2 at the high-symmetry T point is different. At P_2 , the bands belong to two distinct irreducible representations \bar{T}_3 and \bar{T}_4 . Therefore, no gap is observed at the band crossing point P_2 , which implies that LuPb₂ can be considered as a Dirac semimetal. Figure 3(g) presents the magnified view at point P_2 . It is evident that the bands near the T point, and along the T-Y and T-E path directions, exhibit a linear energy-momentum dispersion relation. However, the energy-momentum dispersion along the T-Z direction (k_z direction) is quadratic. Thus, the crossing point at P_2 can be considered as a semi-Dirac point, which has been discussed in the literature [51,52]. The semi-Dirac point is located at 171 meV above the Fermi level, which is comparable to that of the Dirac semimetal Cd₃As₂ (~ 200 meV) [53,54]. In addition, as shown in Fig. 3(h), there are two Dirac nodal lines in the $k_y = \pi, -\pi$ plane, respectively. We further examine the reliability of the nodal line electronic state in the Supplemental Material [55].

Figures 3(c)–3(e) shows the calculated Fermi surface of LuPb₂. These results clearly demonstrate that LuPb₂ is a multiband system with a complex Fermi surface composed of multiple sheets. The pockets are labeled as β , α , and γ in the red dashed boxes in Figs. 3(c)–3(e). As shown in Table III, the calculated Fermi wave vector k_F and effective mass m^* of the γ and β pockets are consistent with the results derived from the oscillation components F_γ and F_β . The effective mass m^* was calculated using the relation $m^* = \frac{\hbar^2}{2\pi} \frac{\partial A_F}{\partial E} |_{E_F}$ [56], where A_F is the cross-sectional area of the Fermi surface, \hbar is the reduced Planck constant, and E_F is the Fermi energy. Given the absence of smaller Fermi pockets, the F_α observed in the dHvA experiment is posited to correspond to the extremal cross section of the bottleneck-shaped Fermi surface depicted in Fig. 3(d). This open orbit is consistent with the scenario

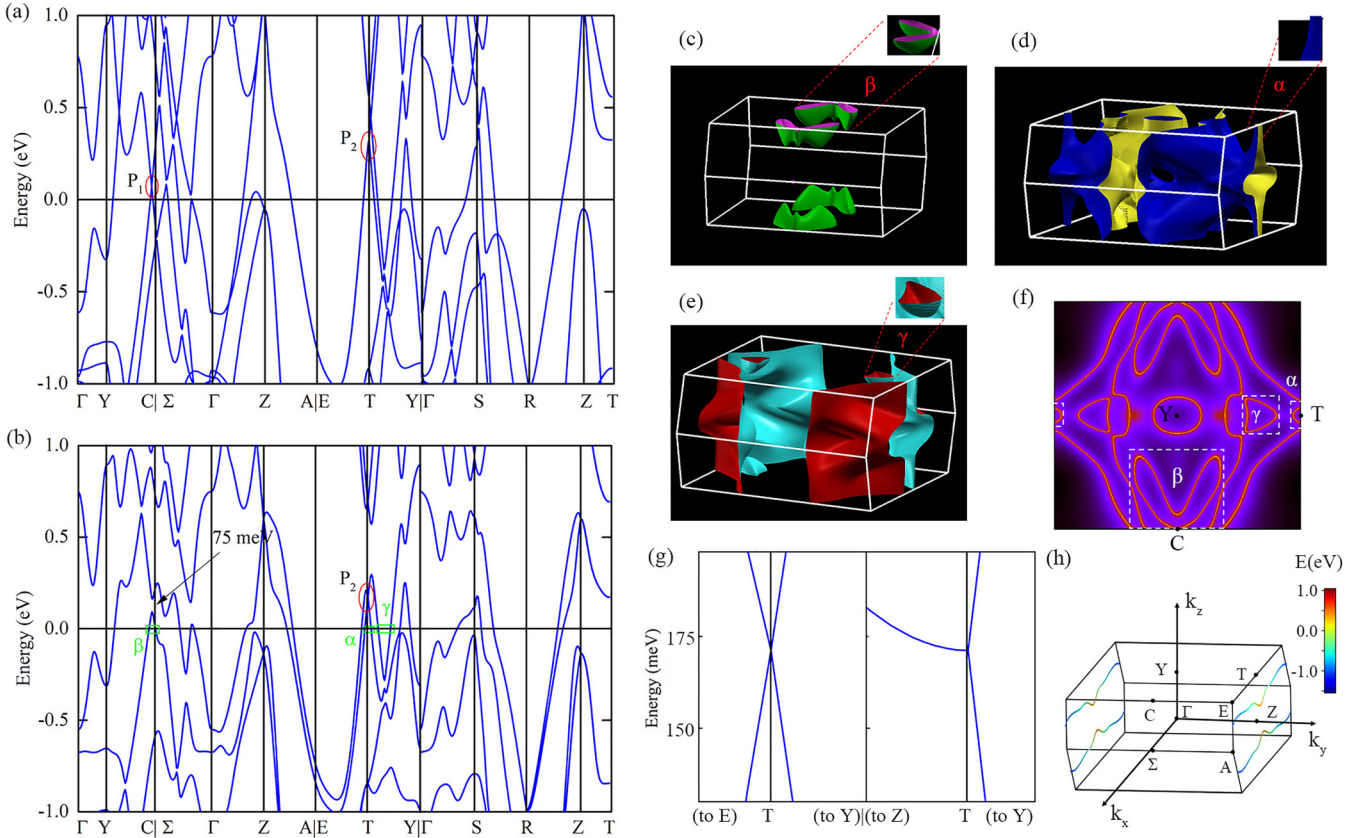


FIG. 3. (a), (b) Electronic band structures for LuPb₂ without and with SOC. The red circles represent the crossing points P₁ and P₂ of the energy bands. The green box highlights the positions of Fermi pockets β , α , and γ . (c)–(e) Multiple FS sheets of LuPb₂. (f) The Fermi surface on the $k_z = \pi$ plane. (g) An expanded view of the band structure near E_F around T (indicated by the circle) is shown, where a band crossing is found ~ 171 meV above the Fermi energy. (h) The first Brillouin zone of LuPb₂, where high-symmetry points and nodal line are marked.

in which F_α only emerges at low angles, as demonstrated in Fig. 2(h). Although the theoretical Fermi wave vector is larger than the experimental value, this discrepancy could be ascribed to self-doping of the grown single crystal. Furthermore, the smaller Fermi pocket α is relatively sensitive to variations in Fermi energy. Figures 3(c)–3(e) also revealed several larger Fermi pockets. Nevertheless, it is possible that the lower mobility of quasiparticles within these pockets prevented their clear resolution in dHvA oscillations. Figure 3(f) shows the Fermi surfaces at $k_z = \pi$, from which the Fermi wave vectors of the three Fermi pockets can be calculated. The β pocket is situated along the Y-C path, while the γ and α pockets reside on the Y-T path. Their positions are indicated by green boxes in Fig. 3(b). It indicates that the α and β pockets are hole type, while the γ pocket is electronic type. Besides, the calculations suggest that the α pocket is related to Dirac crossing band at

the T points, which further suggests the existence of nontrivial topological electronic states in LuPb₂.

D. Quasilinear magnetoresistance and Hall measurement

Figure 4(a) displays the temperature dependence of resistivity from 300 K down to 2 K in zero fields with current applied along the a axis. Figure 4(b) below 30 K shows the best fit by $\rho = \rho_0 + AT^2$ with $A = 7.5 \times 10^{-3} \mu\Omega \text{ cm/K}^2$, indicating that electron-electron scattering dominates low-temperature transport in the compound. Moreover, we observed a residual resistivity ratio of around 52, indicating a high-quality single crystal. Figure 4(c) presents the magnetoresistance ($\text{MR} = [\rho(B) - \rho(0)]/\rho(0) \times 100\%$) dependence of the magnetic field applied along the b axis. At low magnetic fields, the MR exhibits a quadratic

TABLE III. Fermi wave vector and effective mass obtained from the first-principles calculations and dHvA experiments for the α , β , and γ pockets.

Pocket name	dHvA frequencies $F_x(T)$ for $B \parallel b$	k_F (\AA^{-1}) estimated from the dHvA	k_F (\AA^{-1}) DFT-calculated	(m^*/m_0) estimated from the dHvA	(m^*/m_0) DFT-calculated
α	111	0.0580	0.0402	0.179	0.066
β	1041	0.178	0.166	0.355	0.437
γ	233	0.0841	0.0867	0.225	0.146

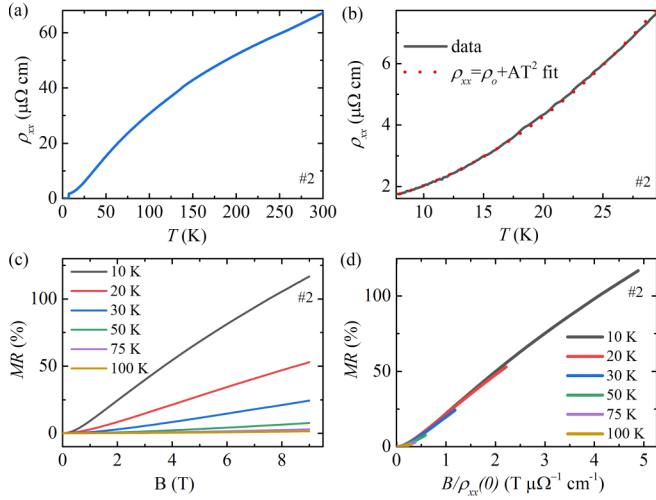


FIG. 4. (a) Zero-field ρ_{xx} as a function of T from 2 K to 300 K. (b) The low-temperature part of ρ_{xx} and its fit with $\rho_{xx} = \rho_0 + AT^2$ ($\rho_0 = 1.29 \mu\Omega \text{ cm}$, $A = 0.0075 \mu\Omega \text{ cm K}^{-2}$). (c) MR dependence of B at different temperatures. (d) Kohler's plot of the MR at different temperatures.

dependence, similar to previous observations in WTe_2 [57] and Gd_3As_2 [58]. The quadratic MR is induced by the Lorenz deflection of carriers under the magnetic field. As the magnetic field increases, the quadratic MR becomes approximately linear, with no signs of saturation. At the field of 9 T, the magnetoresistance exhibited a remarkable increase, rising from 1.4% at $T = 100 \text{ K}$ to nearly 120% at a low temperature of $T = 10 \text{ K}$. Figure 4(d) presents the Kohler plot, in which the MR ratio is plotted as a function of $B/\rho_{xx}(0)$. Below 50 K, the MR curves can be nearly scaled to a single universal curve, indicating a single relevant scattering process is dominant in LuPb_2 .

To further investigate the observed LMR in LuPb_2 , we have performed the Hall effect measurements with the magnetic field along the b axis and the current along the a axis. Figure 5(a) shows the field dependence of the Hall resistivity ρ_{xy} over a temperature range of 10 K to 100 K. The temperature-dependent behavior of ρ_{xy} exhibits a positive dependence on the magnetic field across the entire temperature range, indicating the predominance of hole carriers. The Hall resistivity ρ_{xy} showed nonlinearity at low magnetic fields, suggesting that two types of charge carriers were involved. We employed a two-carrier model to fit the Hall conductivity $\sigma_{xy} = -\frac{\rho_{xy}}{\rho_{xx}^2 + \rho_{xy}^2}$ and imposed an additional restriction by using the zero-field longitudinal conductivity $\sigma_{xx} = \frac{\rho_{xx}}{\rho_{xx}^2 + \rho_{xy}^2}$. Figure 5(b) displays the best-fitting result within the magnetic field range of -9 T to 9 T ,

$$\sigma_{xy} = eB \left(\frac{n_e \mu_e^2}{1 + (\mu_e B)^2} - \frac{n_h \mu_h^2}{1 + (\mu_h B)^2} \right). \quad (2)$$

The two-carrier model fits σ_{xy} well from 10 K to 100 K. The temperature dependence of carrier densities and mobility obtained by fitting are shown in Figs. 5(c) and 5(d), respectively. At 10 K, n_h was larger than n_e , indicating incomplete electron-hole compensation and hole dominance at low temperatures. The densities on the order of 10^{20} cm^{-3} imply

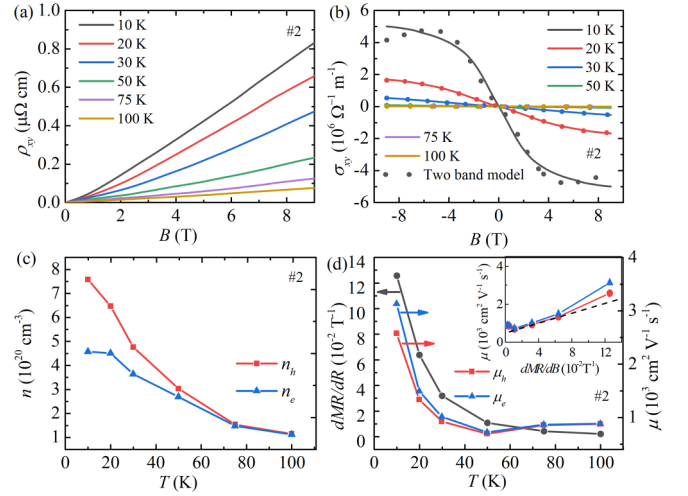


FIG. 5. (a) ρ_{xy} as a function of B at different temperatures. (b) Magnetic field dependence of Hall conductivity σ_{xy} at various temperatures. The dashed lines present the good fitting result of the two-band model. (c) The temperature dependence of the calculated carrier density. (d) Mobility μ (right axis) and $d\text{MR}/dB$ (left axis) dependence of T . The inset shows the $d\text{MR}/dB$ dependence of mobility. The dotted line is the guiding line.

the concentration of semimetal. They also agreed with those calculated from the quantum oscillations of the β band. Both μ_h and μ_e decrease with increasing temperature. We note that the transport mobility μ was larger than the quantum mobility μ_q derived from quantum oscillations. The quantum mobility μ_q was sensitive to both small-angle and large-angle scattering, whereas the transport mobility μ was mainly sensitive to large-angle scattering only [32,59].

The phenomenon of LMR can be partially explained through the application of both classical and quantum models. According to the linear quantum MR model developed by Abrikosov [31,60], LMR is observed in the quantum limit $\hbar\omega_c > E_F$ when all the charge carriers are confined into the lowest Landau levels, where ω_c is the cyclotron frequency and E_F is the Fermi energy. However, the LMR here already exists at the low field and the dHvA effect measurement indicates that even with a 9 T magnetic field applied, the lowest Landau level is not achieved in the smallest pocket α . Therefore the observed LMR should not be attributed to the quantum model. On the other hand, the 3D larger β Fermi pocket with higher light carrier density would dominate the transport behavior. As a result, the open-orbit scenario is at odds with a linear field-dependent MR.

Subsequently, the classical PL model [22] is employed to account for the LMR. According to the model, a disordered conducting system is viewed as an infinite network of small four-terminal van der Pauw resistors. A high magnetic field, when applied, compels the majority of the current to flow in a direction perpendicular to the applied voltage, resulting in a linear field-dependent Hall resistance contribution to effective magnetoresistance. Once there is an application of an external field perpendicular to the network's plane, either the width of the mobility disorder $\Delta\mu$ or average mobility $\langle\mu\rangle$ dominate the linear MR. In Fig. 5(c), there is a high carrier

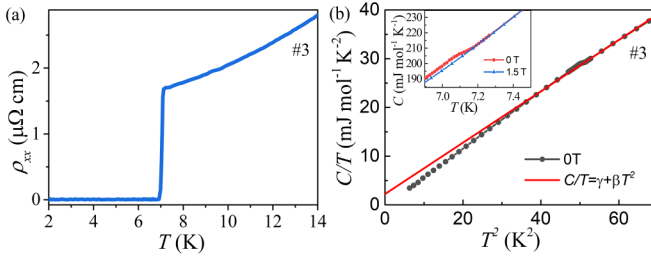


FIG. 6. (a) Temperature dependence of the superconducting and normal-state resistivity for LuPb₂ between 2 K and 14 K with the measuring current applied along the [100] crystal direction. LuPb₂ has a superconducting transition at $T_c = 7.2$ K. (b) C/T as a function of T^2 at zero fields (black line). The red solid line represents the fit to the equation $C/T = \gamma + \beta T^2$. The inset shows the specific heat C dependence of temperature at $B = 0$ T and $B = 1.5$ T.

concentration $\sim 10^{20}$ cm⁻³, which could partially screen the spatial fluctuations of mobility by the disorder. Therefore, the fluctuations of mobility $\Delta\mu$ should be smaller than the average mobility $\langle\mu\rangle$ at low temperature. In this case, the classical model expects that the slope of magnetoresistance at high fields should be proportional to average mobility $\langle\mu\rangle$. Figure 5(d) presented the first-order derivative of MR in high magnetic fields, denoted on the left axis. Additionally, the values of μ for both electrons and holes are shown on the right axis. As a result, the behavior of dMR/dB with respect to temperature does appear to be similar to that of μ_e and μ_h below 50 K. The inset of Fig. 5(d) demonstrates the close linear relationship between the carrier mobility and dMR/dB . Below 50 K, hole carriers serve as the majority carriers and thus display a more linear dependence compared to electron carriers. At temperatures above 50 K, the hole and electronic carriers approach perfect compensation, which may lead to a reduced contribution of the Hall resistance to the effective magnetoresistance. As a result, the dependence of carrier mobility μ on dMR/dB begins to deviate from linearity. At the same time, this also causes the dependence not to be strictly proportional [61,62]. Therefore, the observed results satisfy the conditions for the weak mobility fluctuation limit of the PL model. The LMR in LuPb₂ is most likely attributed to the classical origin.

E. Superconductivity

We turn to the observed superconductivity in the sample. Figure 6(a) shows the sharp superconducting transition below the temperature of $T = 7.2$ K, which is close to that of pure lead. To further characterize the superconductivity of LuPb₂, we conducted temperature-dependent specific-heat measurements at $B = 0$ T and $B = 1.5$ T, as shown in inset of Fig. 6(b). The specific heat shows a small jump ($\Delta C \sim 3$ mJ mol⁻¹ K⁻¹) at the critical temperature of $T_c \sim 7.17$ K under zero field. Above the transition temperature, the data are well described by $C/T = \gamma + \beta T^2$ in Fig. 6(b) and yield the Sommerfeld coefficient $\gamma = 2.22 \pm 0.16$ mJ mol⁻¹ K⁻², $\beta = 0.527 \pm 0.004$ mJ mol⁻¹ K⁻⁴. We find the value of $\Delta C/\gamma T_c$ to be 0.19, which is significantly below the BCS limit of 1.43 for weakly coupled superconductors. This discrepancy suggests

that the observed superconductivity in the sample may not be intrinsic.

The Meissner effect measurements further confirm the superconductivity in the sample. Figure 7(a) shows the temperature dependence of the DC magnetic susceptibility in a field of 100 Oe applied along the b axis and ac plane. Note that the effective magnetic susceptibility $\chi_{dc} = \chi/(1 - N)$ was obtained with a demagnetization factor $N_{\perp} = 0.18$ for $B \perp b$ axis and $N_{\parallel} = 0.8$ for $B \parallel b$ axis. Nevertheless, we obtained $\chi_{B\parallel b} = -1$ and $\chi_{B\perp b} = -0.8$ at $T = 2$ K. The observation that the volume fraction of the superconducting state in the sample is nearly 100% suggests the manifestation of bulk superconductivity properties. However, the low value of $\Delta C/\gamma T_c$ mentioned earlier implies that the high volume fraction of superconductivity determined by the Meissner effect may also be attributed to the shell effect [63,64].

Figures 7(b) and 7(f) show the isothermal magnetization for $B \parallel b$ axis and $B \perp b$ axis, respectively. The Meissner fraction induced by the superconducting state undergoes a significant reduction in several hundred Oe and eventually disappears at approximately 2 kOe for $B \parallel b$ and 4 kOe for $B \perp b$. The critical field anisotropy in the sample is different from that of pure bulk lead with isotropic properties. Figures 7(c) and 7(g) present the temperature dependence of longitudinal resistivity ρ_{xx} under fields applied along the ac plane and b axis, respectively. Notably, the resistivity critical field is nearly one order of magnitude higher than that observed in magnetization, in addition to its anisotropy. This phenomenon of resistivity critical field enhancement has been previously observed in other superconducting materials, such as BeAu [65], BiPd [66], and LaPtSi₃, all of which are type I or I/II superconductors with upper critical fields ranging between 100 and 1000 Oe. However, the upper critical field in LuPb₂ is distinctly one order of magnitude larger than these materials.

Considering that surface superconductivity may be a potential explanation for the observed enhancement of critical field, it is assumed here that the upper critical field obtained from resistivity measurements corresponds to the surface critical field B_{c3} . Figures 7(e), 7(d), and 7(h) show the temperature-dependent lower critical field B_{c1} , upper critical field B_{c2} , and surface critical field B_{c3} , respectively. The lower critical field, B_{c1} , is defined as the field at which the $M(H)$ curves first deviate from linear behavior. The data can be well described by the Ginzburg-Landau (GL) expression $B_{c1}(t) = B_{c1}(0)(1 - t^2)$, where $t = T/T_c$. The estimated critical fields $B_{c1}(0)(B \perp b)$ and $B_{c1}(0)(B \parallel b)$ are 259 and 187 Oe, respectively. The field corresponding to 10% of the maximum magnetization value is defined as B_{c2} . The data were analyzed using the Ginzburg-Landau (GL) formula, where $B_{c2}(t) = B_{c2}(0)(1 - t^2)(1 + t^2)$. The estimated critical fields $B_{c2}(0)(B \perp b)$ and $B_{c2}(0)(B \parallel b)$ were found to be 0.43 T and 0.1 T, respectively. The field corresponding to 90% of the normal-state resistivity was defined as B_{c3} . Due to the unusual shape of the curve, we estimated the value of $B_{c3}(0)$ by fitting the GL formula $B_{c3}(t) = B_{c3}(0)(1 - t^2)$. The obtained values of $B_{c3}(0)$ are 4.2 T and 1.1 T for $B \perp b$ and $B \parallel b$, respectively. The calculated ratios B_{c3}/B_{c2} are up to 15 and 5.6 for $B \perp b$ and $B \parallel b$, respectively. Notably, both ratios are larger than the Saint-James

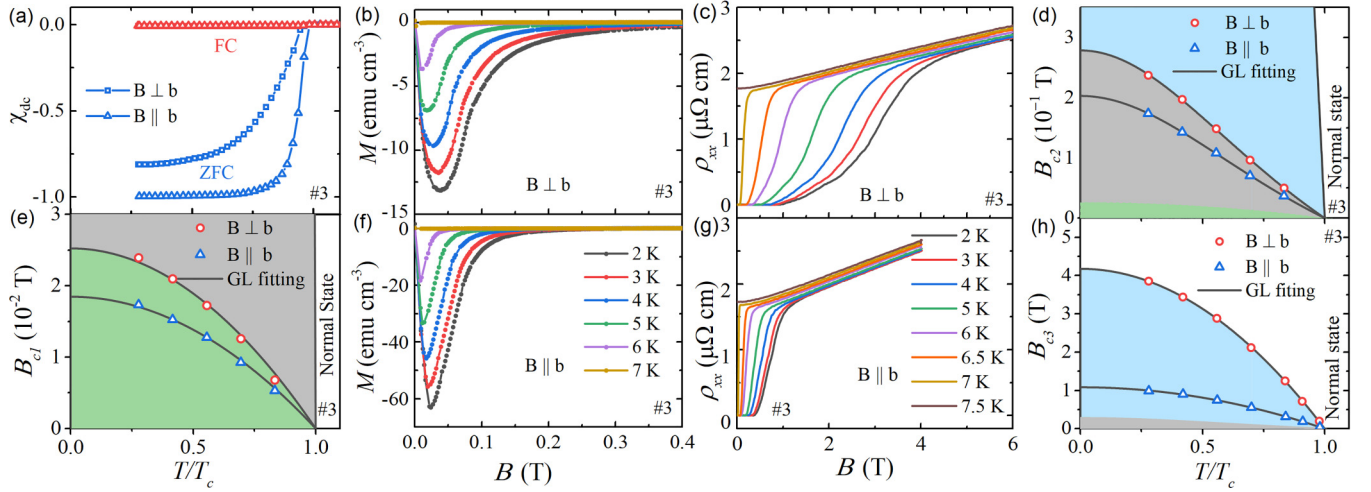


FIG. 7. (a) The ZFC and FC magnetic volume susceptibility under magnetic field $B = 100$ Oe. The ZFC susceptibility saturates to a value of -1 for $B \parallel b$ and -0.82 for $B \perp b$. (b) and (f) DC magnetization M vs magnetic field B at various temperatures for LuPb₂ for both orientations. B_{c1} is the field that deviates from the linear part. (c) and (g) The magnetic field dependence of the superconducting transition temperature is measured at different temperatures. (d) Phase diagram of the upper critical field B_{c2} versus T/T_c for the $B \parallel b$ axis (blue) and $B \perp b$ axis (red). The solid lines show fits to the data using the Ginzburg-Landau formula $B_{c2}(T) = B_{c2}(0)[1 - (T/T_c)^2]/[1 + (T/T_c)^2]$. (e) Phase diagram of lower critical field B_{c1} versus T/T_c . The solid lines show fits to the data using the GL formula $B_{c1}(T) = B_{c1}(0)[1 - (T/T_c)^2]$. (h) Phase diagram showing the temperature dependence of the critical field B_{c3} .

and de Gennes limit [67] of 1.695 for type-II superconductors. This relatively large ratio suggests that the enhancement of resistivity critical field may be dominated by other mechanisms.

The anisotropy and enhancement of the resistivity critical field indicate an interesting anomaly in the superconductivity of the sample. We also note that the critical field can be significantly enhanced in aluminum nanowires [68], small lead particles [69] lead films [70], and (TMTSF)₂CLO₄ and (TMTSF)₂PF₆ nanoparticles [71] compared to bulk materials. This could suggest that the mechanism behind the enhancement critical field in the sample may be connected with quantum size effect [72,73]. According to the theory, when a field is applied parallel to the surface and a film with thickness comparable to the penetration depth is considered, the transition to the normal state occurs at the field $H_{\parallel}(T) = 2\sqrt{6}\lambda_e(T)H_{cb}(T)/d$, where $H_{cb}(T)$, $\lambda_e(T)$, and d represent the bulk critical field, bulk weak field penetration depth [74], and thickness of the film, respectively [75–78]. We estimated that, for the critical upper field of 4.2 T, the thickness of the lead layer on the sample surface is approximately 2.86 nm. However, the superconducting transition shown in Fig. 7(c) exhibits significant broadening, suggesting that the estimated thickness value represents a lower limit. Overall, we believe that the nanoscale lead layer appearing on the ac plane of the sample leads to observations of superconductivity that differ from pure bulk lead. This phenomenological analysis provides some understanding of all low-temperature experimental observations, including the sharp resistivity transition, small specific-heat jump, strong anisotropy of critical field, large superconducting volume fraction, and broadening of the superconducting transition. However, the underlying mechanism that governs the occurrence of a nanoscale lead layer exclusively on the ac plane of the sample remains unclear.

Besides that, this kind of microstructure has not been directly observed. Although we attempted TEM experiments, we did not receive good experimental results due to the air sensitivity of the sample. Further investigation is warranted to unravel the intricate details of this phenomenon and address these lingering questions that persist.

IV. CONCLUSION

In conclusion, we have successfully synthesized high-quality LuPb₂ single crystals. The observation of clear quantum oscillations in the dHvA experiment has confirmed the 3D Fermi characteristics and nontrivial Berry phase. Our DFT calculations further confirm the existence of Dirac linear energy-momentum dispersion in the α band, suggesting that LuPb₂ could be a topologically nontrivial material. Furthermore, our investigation of the magnetotransport properties of LuPb₂ single crystals revealed a quasilinear MR at high magnetic fields. Our analysis suggests that this quasilinear MR is primarily governed by the average mobility of charge carriers. Moreover, we have observed the presence of surface superconductivity with a highly anisotropic upper critical field and enhancement of the resistivity critical field, which we attribute to a potential nanostructured lead layer on the sample surface.

ACKNOWLEDGMENTS

This work is supported by the National Science Foundation of China (Grants No. 12004123, No. 51861135104, No. 11574097, and No. 12274154), the National Key Research and Development Program of China (Grant No. 2022YFA1403500), and the Fundamental Research Funds for the Central Universities (Grant No. 2019kfyXMBZ071).

- [1] S. Klemenč, S. Lei, and L. M. Schoop, *Annu. Rev. Mater. Res.* **49**, 185 (2019).
- [2] K. Wang, D. Graf, L. Wang, H. Lei, S. W. Tozer, and C. Petrovic, *Phys. Rev. B* **85**, 041101(R) (2012).
- [3] Y. Feng, Z. Wang, C. Chen, Y. Shi, Z. Xie, H. Yi, A. Liang, S. He, J. He, Y. Peng, X. Liu, Y. Liu, L. Zhao, G. Liu, X. Dong, J. Zhang, C. Chen, Z. Xu, X. Dai, Z. Fang, and X. J. Zhou, *Sci. Rep.* **4**, 5385 (2014).
- [4] L. Li, K. Wang, D. Graf, L. Wang, A. Wang, and C. Petrovic, *Phys. Rev. B* **93**, 115141 (2016).
- [5] A. Zhang, C. Liu, C. Yi, G. Zhao, T.-L. Xia, J. Ji, Y. Shi, R. Yu, X. Wang, C. Chen, and Q. Zhang, *Nat. Commun.* **7**, 13833 (2016).
- [6] L. M. Schoop, M. N. Ali, C. Straßer, A. Topp, A. Varykhalov, D. Marchenko, V. Duppel, S. S. Parkin, B. V. Lotsch, and C. R. Ast, *Nat. Commun.* **7**, 11696 (2016).
- [7] J. Hu, Z. Tang, J. Liu, X. Liu, Y. Zhu, D. Graf, K. Myhro, S. Tran, C. N. Lau, J. Wei, and Z. Mao, *Phys. Rev. Lett.* **117**, 016602 (2016).
- [8] M. M. Hosen, K. Dimitri, I. Belopolski, P. Maldonado, R. Sankar, N. Dhakal, G. Dhakal, T. Cole, P. M. Oppeneer, D. Kaczorowski, F. Chou, M. Z. Hasan, T. Durakiewicz, and M. Neupane, *Phys. Rev. B* **95**, 161101(R) (2017).
- [9] Y. Zhu, T. Zhang, J. Hu, J. Kidd, D. Graf, X. Gui, W. Xie, M. Zhu, X. Ke, H. Cao, Z. Fang, H. Weng, and Z. Mao, *Phys. Rev. B* **98**, 035117 (2018).
- [10] Y. Zhu, J. Hu, D. Graf, X. Gui, W. Xie, and Z. Mao, *Phys. Rev. B* **103**, 125109 (2021).
- [11] Y. Chen, F. Tang, W. Z. Meng, X. Shen, W. Zhao, X. Q. Yin, S. Cong, Q. H. Yi, L. Zhang, D. J. Wu, Z.-D. Han, B. Qian, X.-F. Jiang, X. M. Zhang, and Y. Fang, *Phys. Rev. B* **104**, 165128 (2021).
- [12] L. M. Schoop, A. Topp, J. Lippmann, F. Orlandi, L. Muehler, M. G. Vergniory, Y. Sun, A. W. Rost, V. Duppel, M. Krivenkov *et al.*, *Sci. Adv.* **4**, eaar2317 (2018).
- [13] R. J. Cava, *J. Am. Ceram. Soc.* **83**, 5 (2000).
- [14] S. Ishizaka, A. Ino, T. Kono, Y. Miyai, S. Kumar, K. Shimada, H. Kitô, I. Hase, S. Ishida, K. Oka, H. Fujihisa, Y. Gotoh, Y. Yoshida, A. Iyo, H. Ogino, H. Eisaki, K. Kawashima, Y. Yanagi, and A. Kimura, *Phys. Rev. B* **105**, L121103 (2022).
- [15] H. Mizoguchi, S. Matsuishi, M. Hirano, M. Tachibana, E. Takayama-Muromachi, H. Kawaji, and H. Hosono, *Phys. Rev. Lett.* **106**, 057002 (2011).
- [16] K. Górnicka, S. Gutowska, M. J. Winarski, B. Wiendlocha, W. Xie, R. Cava, and T. Klimczuk, *Chem. Mater.* **32**, 3150 (2020).
- [17] A. B. Pippard, *Magnetoresistance in Metals* (Cambridge University Press, Cambridge, 1989).
- [18] M. N. Ali, J. Xiong, S. Flynn, J. Tao, Q. D. Gibson, L. M. Schoop, T. Liang, N. Haldolaarachchige, M. Hirschberger, N. P. Ong *et al.*, *Nature (London)* **514**, 205 (2014).
- [19] P.-J. Guo, H.-C. Yang, B.-J. Zhang, K. Liu, and Z.-Y. Lu, *Phys. Rev. B* **93**, 235142 (2016).
- [20] F. Yang, K. Liu, K. Hong, D. Reich, P. Searson, and C. Chien, *Science* **284**, 1335 (1999).
- [21] J. Hu and T. F. Rosenbaum, *Nat. Mater.* **7**, 697 (2008).
- [22] M. Parish and P. Littlewood, *Nature (London)* **426**, 162 (2003).
- [23] A. L. Friedman, J. L. Tedesco, P. M. Campbell, J. C. Culbertson, E. Aifer, F. K. Perkins, R. L. Myers-Ward, J. K. Hite, C. R. Eddy Jr., G. G. Jernigan *et al.*, *Nano Lett.* **10**, 3962 (2010).
- [24] Z.-M. Liao, H.-C. Wu, S. Kumar, G. S. Duesberg, Y.-B. Zhou, G. L. Cross, I. V. Shvets, and D.-P. Yu, *Adv. Mater.* **24**, 1862 (2012).
- [25] F. Kisslinger, C. Ott, C. Heide, E. Kampert, B. Butz, E. Spiecker, S. Shallcross, and H. B. Weber, *Nat. Phys.* **11**, 650 (2015).
- [26] B. Wu, V. Barrena, H. Suderow, and I. Guillamón, *Phys. Rev. Res.* **2**, 022042(R) (2020).
- [27] W. Wang, Y. Du, G. Xu, X. Zhang, E. Liu, Z. Liu, Y. Shi, J. Chen, G. Wu, and X.-X. Zhang, *Sci. Rep.* **3**, 2181 (2013).
- [28] X. Huang, L. Zhao, Y. Long, P. Wang, D. Chen, Z. Yang, H. Liang, M. Xue, H. Weng, Z. Fang, X. Dai, and G. Chen, *Phys. Rev. X* **5**, 031023 (2015).
- [29] J. Xiong, S. Kushwaha, J. Krizan, T. Liang, R. J. Cava, and N. P. Ong, *Europhys. Lett.* **114**, 27002 (2016).
- [30] X. Wang, Y. Du, S. Dou, and C. Zhang, *Phys. Rev. Lett.* **108**, 266806 (2012).
- [31] A. A. Abrikosov, *Phys. Rev. B* **58**, 2788 (1998).
- [32] A. Narayanan, M. D. Watson, S. F. Blake, N. Bruyant, L. Drigo, Y. L. Chen, D. Prabhakaran, B. Yan, C. Felser, T. Kong, P. C. Canfield, and A. I. Coldea, *Phys. Rev. Lett.* **114**, 117201 (2015).
- [33] M. Novak, S. Sasaki, K. Segawa, and Y. Ando, *Phys. Rev. B* **91**, 041203(R) (2015).
- [34] T. Khouri, U. Zeitler, C. Reichl, W. Wegscheider, N. E. Hussey, S. Wiedmann, and J. C. Maan, *Phys. Rev. Lett.* **117**, 256601 (2016).
- [35] P. Hohenberg and W. Kohn, *Phys. Rev.* **136**, B864 (1964).
- [36] J. P. Perdew, K. Burke, and M. Ernzerhof, *Phys. Rev. Lett.* **77**, 3865 (1996).
- [37] G. Kresse and D. Joubert, *Phys. Rev. B* **59**, 1758 (1999).
- [38] G. Kresse and J. Furthmüller, *Phys. Rev. B* **54**, 11169 (1996).
- [39] N. Marzari and D. Vanderbilt, *Phys. Rev. B* **56**, 12847 (1997).
- [40] Q. Wu, S. Zhang, H.-F. Song, M. Troyer, and A. A. Soluyanov, *Comput. Phys. Commun.* **224**, 405 (2018).
- [41] G. Borzone, N. Parodi, R. Ferro, M. Gambino, V. Vassiliev, and J. P. Bros, *J. Alloys Compd.* **220**, 111 (1995).
- [42] O. D. McMasters Jr. and K. Gschneidner Jr., *J. Less-Common Met.* **19**, 337 (1969).
- [43] P. M. Everett and C. G. Grenier, *Phys. Rev. B* **15**, 3826 (1977).
- [44] U. Ivowi and L. Mackinnon, *J. Phys. F* **6**, 329 (1976).
- [45] D. Shoenberg, *Magnetic Oscillations in Metals* (Cambridge University Press, Cambridge, 2009).
- [46] B. J. Lawson, Y. S. Hor, and L. Li, *Phys. Rev. Lett.* **109**, 226406 (2012).
- [47] M. N. Ali, L. M. Schoop, C. Garg, J. M. Lippmann, E. Lara, B. Lotsch, and S. S. Parkin, *Sci. Adv.* **2**, e1601742 (2016).
- [48] J. Xiong, Y. Luo, Y. H. Khoo, S. Jia, R. J. Cava, and N. P. Ong, *Phys. Rev. B* **86**, 045314 (2012).
- [49] A. Alexandradinata, C. Wang, W. Duan, and L. Glazman, *Phys. Rev. X* **8**, 011027 (2018).
- [50] C. Guo, A. Alexandradinata, C. Putzke, A. Estry, T. Tu, N. Kumar, F.-R. Fan, S. Zhang, Q. Wu, O. V. Yazyev *et al.*, *Nat. Commun.* **12**, 6213 (2021).
- [51] S. Banerjee, R. R. P. Singh, V. Pardo, and W. E. Pickett, *Phys. Rev. Lett.* **103**, 016402 (2009).
- [52] P. Dietl, F. Piéchon, and G. Montambaux, *Phys. Rev. Lett.* **100**, 236405 (2008).
- [53] M. Neupane, S.-Y. Xu, R. Sankar, N. Alidoust, G. Bian, C. Liu, I. Belopolski, T.-R. Chang, H.-T. Jeng, H. Lin *et al.*, *Nat. Commun.* **5**, 3786 (2014).

- [54] S. Jeon, B. B. Zhou, A. Gyenis, B. E. Feldman, I. Kimchi, A. C. Potter, Q. D. Gibson, R. J. Cava, A. Vishwanath, and A. Yazdani, *Nat. Mater.* **13**, 851 (2014).
- [55] See Supplemental Material at <http://link.aps.org/supplemental/10.1103/PhysRevB.108.035137> for validation of nodal line.
- [56] J. M. Ziman, *Principles of the Theory of Solids* (Cambridge University Press, Cambridge, 1972).
- [57] Y. Zhao, H. Liu, J. Yan, W. An, J. Liu, X. Zhang, H. Wang, Y. Liu, H. Jiang, Q. Li, Y. Wang, X.-Z. Li, D. Mandrus, X. C. Xie, M. Pan, and J. Wang, *Phys. Rev. B* **92**, 041104(R) (2015).
- [58] L. P. He, X. C. Hong, J. K. Dong, J. Pan, Z. Zhang, J. Zhang, and S. Y. Li, *Phys. Rev. Lett.* **113**, 246402 (2014).
- [59] Q. Chen, Z. Lou, S. N. Zhang, B. Xu, Y. Zhou, H. Chen, S. Chen, J. Du, H. Wang, J. Yang, Q. S. Wu, O. V. Yazyev, and M. Fang, *Phys. Rev. B* **102**, 165133 (2020).
- [60] A. Abrikosov, *Europhys. Lett.* **49**, 789 (2000).
- [61] W. L. Zhu, Y. Cao, P. J. Guo, X. Li, Y. J. Chen, L. J. Zhu, J. B. He, Y. F. Huang, Q. X. Dong, Y. Y. Wang, R. Q. Zhai, Y. B. Ou, G. Q. Zhu, H. Y. Lu, G. Li, G. F. Chen, and M. H. Pan, *Phys. Rev. B* **105**, 125116 (2022).
- [62] V. Saini, S. Sasmal, R. Kulkarni, and A. Thamizhavel, *Appl. Phys. Lett.* **119**, 071904 (2021).
- [63] S. Bose, A. M. García-García, M. M. Ugeda, J. D. Urbina, C. H. Michaelis, I. Brihuega, and K. Kern, *Nat. Mater.* **9**, 550 (2010).
- [64] L. Dong, H. Zhao, I. Zeljkovic, S. D. Wilson, and J. W. Harter, *Phys. Rev. Mater.* **3**, 114801 (2019).
- [65] D. J. Rebar, S. M. Birnbaum, J. Singleton, M. Khan, J. C. Ball, P. W. Adams, J. Y. Chan, D. P. Young, D. A. Browne, and J. F. DiTusa, *Phys. Rev. B* **99**, 094517 (2019).
- [66] D. C. Peets, A. Maldonado, M. Enayat, Z. Sun, P. Wahl, and A. P. Schnyder, *Phys. Rev. B* **93**, 174504 (2016).
- [67] D. Saint-James and P. de Gennes, *Phys. Lett.* **7**, 306 (1963).
- [68] M. Singh, J. Wang, M. Tian, Q. Zhang, A. Pereira, N. Kumar, T. E. Mallouk, and M. H. Chan, *Chem. Mater.* **21**, 5557 (2009).
- [69] S. Reich, G. Leitus, R. Popovitz-Biro, and M. Schechter, *Phys. Rev. Lett.* **91**, 147001 (2003).
- [70] Y. Liu, Z. Wang, X. Zhang, C. Liu, Y. Liu, Z. Zhou, J. Wang, Q. Wang, Y. Liu, C. Xi, M. Tian, H. Liu, J. Feng, X. C. Xie, and J. Wang, *Phys. Rev. X* **8**, 021002 (2018).
- [71] L. E. Winter, E. Steven, J. S. Brooks, S. Benjamin, J.-H. Park, D. de Caro, C. Faulmann, L. Valade, K. Jacob, I. Chtioui, B. Ballesteros, and J. Fraxedas, *Phys. Rev. B* **91**, 035437 (2015).
- [72] W. P. Halperin, *Rev. Mod. Phys.* **58**, 533 (1986).
- [73] X.-Y. Bao, Y.-F. Zhang, Y. Wang, J.-F. Jia, Q.-K. Xue, X. C. Xie, and Z.-X. Zhao, *Phys. Rev. Lett.* **95**, 247005 (2005).
- [74] R. F. Gasparovic and W. L. McLean, *Phys. Rev. B* **2**, 2519 (1970).
- [75] M. Tinkham, *Phys. Rev.* **129**, 2413 (1963).
- [76] S. L. Prischepa, C. Cirillo, V. N. Kushnir, E. A. Ilyina, M. Salvato, and C. Attanasio, *Phys. Rev. B* **72**, 024535 (2005).
- [77] S. Kittaka, T. Nakamura, Y. Aono, S. Yonezawa, K. Ishida, and Y. Maeno, *Phys. Rev. B* **80**, 174514 (2009).
- [78] A. K. Ghosh, M. Tokunaga, and T. Tamegai, *Phys. Rev. B* **68**, 054507 (2003).